

The effect of geographic sampling on extreme precipitation: from models to observations and back again

Mark D. Risser and Michael F. Wehner

Abstract

In light of the significant uncertainties present in global climate models’ characterization of precipitation extremes, it is important to properly use observational data sets to determine whether a particular climate model is suitable for simulating extremes. In this paper, we identify two problems with traditional approaches for comparing global climate models and observational data products with respect to extremes: first, daily gridded products are a suboptimal data source to use for this comparison, and second, failing to account for the geographic locations of weather station data can paint a misleading picture with respect to model performance. To demonstrate these problems, we utilize in situ measurements of daily precipitation along with a spatial statistical extreme value analysis to evaluate and compare model performance with respect to extreme climatology. As an illustration, we use model output from five early submissions to the HighResMIP subproject of the CMIP6 experiment ([Haarsma et al., 2016](#)), comparing integrated metrics of an “extreme” bias and Taylor diagrams. Our main point is that the choice of methodology for model comparison of extremes (with respect to choice of observational data and accounting for geographic sampling) is relatively unimportant for well-sampled areas but very important for sparsely sampled areas. While we focus on the contiguous United States in this paper, our results have important implications for other global land regions where the sampling problem is more severe.

Keywords: spatial statistics, extreme value analysis, HighResMIP, extreme precipitation, model evaluation, Taylor diagram

1 Introduction

Global climate models can contain significant uncertainties, particularly in their characterization of precipitation extremes. As such, it is critical to use observationally-based data sets to evaluate a particular climate model to assess if the model is fit for purpose in exploring extremes and, if so, where and when the model is either acceptable or unacceptable for characterizing extreme precipitation. Traditionally, gridded daily products are used as a “ground truth” data set for evaluating a climate model because (1) these data products are based on measurements of the real world (e.g., in situ measurements, satellite observations, or reanalysis products) and (2) the products interpolate

daily measurements onto a uniform space-time grid to create a spatially- and temporally-complete version of the raw data, which makes comparison much more straightforward.

However, we assert that there are two problems with this approach when considering precipitation extremes. First, a recent thread of research argues that gridded daily products are an inappropriate data source for characterizing extreme precipitation. The reasoning here is that daily precipitation is known to exhibit fractal scaling (see, e.g., [Lovejoy et al., 2008](#); [Maskey et al., 2016](#), and numerous references therein), and therefore any spatial averaging during the gridding process will diminish variability and extreme values. Furthermore, there are an emerging number of analyses that specifically document the inappropriateness of using daily gridded products as a substitute for observed extremes ([King et al., 2013](#); [Gervais et al., 2014](#); [Timmermans et al., 2019](#); [Risser et al., 2019b](#)). Second, for comparison with climate model output, it should be noted that the underlying physics of the climate model yields a process-based characterization of, e.g., extreme precipitation, at every grid cell while gridded products are based on spatially irregular measurements. As such, a comparison of the climate model versus a gridded product over an area with poor observational sampling (e.g., regions with large orographic variability) is likely misleading, since the gridded product does not represent actual measurements of daily precipitation at these locations. This problem is likely to worsen when considering very high resolution gridded products (e.g., [Thornton et al., 2014](#), which has a 1 km horizontal resolution) and/or very high resolution global climate models (e.g., the HadGEM3-GC3.1 model, [Roberts et al., 2019](#), has a ~ 25 km horizontal resolution). In fact, this latter problem has already been examined in constructions of global mean temperature trends from station data ([Madden and Meehl, 1993](#); [Vose et al., 2005](#)), although the effects of geographic sampling were minor partly because of the great care taken in the construction of trends ([Jones et al., 2001](#)).

In this paper, we make the case for two general principles when comparing climate models' representation of extremes to observations: first, gridded daily products are a suboptimal data source, and second, the geographic sampling of observational data should be taken into consideration. While we explore the contiguous United States (CONUS) in this paper, the second principle is particularly important when considering global regions with very limited sampling (e.g., northern Africa). An alternative to gridded daily products is a probabilistic or climatological gridded product based on the methodology of [Risser et al. \(2019b\)](#), which applies smoothing techniques to climatological properties instead of daily weather. Their methodology solved a longstanding problem in climate model evaluation by demonstrating that the appropriate comparison is statistics versus statistics: statistics (or the climatology) are what models are designed to capture, as opposed to a particular stochastic time series. Furthermore, the methodology in [Risser et al. \(2019b\)](#) involves a spatial analysis that both borrows strength to increase the signal-to-noise ratio and provides a data-driven procedure for interpolating irregularly observed measurements. As such, this

methodology allows us to address both of these issues in a single framework: first, we can use in situ measurements for an evaluation of precipitation extremes, and second, the spatial aspect of the methodology allows us to analyze spatially irregular measurements, from either weather stations or a spatial subset of model grid cells. In light of these considerations, here we apply the analysis of [Risser et al. \(2019b\)](#) to both in situ measurements of extreme precipitation as well as the corresponding quantity from climate models. As a result, we demonstrate that using gridded daily products can paint a misleading picture with respect to the skill of climate models’ representation of extremes, but that use of a spatial analysis for models and observations yields a closer match relative to an analysis that only accounts for geographic sampling.

The paper proceeds as follows: in Section 2 we describe the various data sources used (in situ, gridded daily products, and climate model output) in our analysis, and in Section 3 we describe the statistical methods. In Section 4, we illustrate our methodology using a case study comparing a well-sampled (spatially) region versus a poorly-sampled region before presenting the results of our analysis for all of CONUS, maintaining a focus on Boreal winter (DJF) precipitation. Section 5 concludes the paper.

2 Data sources

2.1 In situ weather station measurements

The station data used for the following analysis consist of daily measurements of total precipitation (in millimeters) obtained from the Global Historical Climatology Network (GHCN; [Menne et al., 2012](#)) over the contiguous United States (CONUS). We refer the reader to [Risser et al. \(2019b\)](#) for details on the quality assurance procedure. After pre-processing the daily values, we select the subset of stations that have a minimum of 66.7% nonmissing daily precipitation measurements between December 1, 1949 through November 30, 2017. This procedure yields a high-quality set of daily precipitation measurements for $n = 5202$ stations shown in Figure A.1 down-selected from the entire GHCN database of over twenty thousand weather stations with measurements spanning this time period. For these stations, we then extract the largest running 5-day precipitation total (denoted Rx5Day) in DJF for all years with less than 33.3% missing daily values; this yields the values

$$\{Y_t^G(\mathbf{s}) : t = 1950, \dots, 2014; \mathbf{s} \in \mathcal{G}_G\},$$

where \mathcal{G}_G denotes the $n = 5202$ GHCN stations shown in Figure A.1, which are used for the analyses in this paper. Note that [Risser et al. \(2019b\)](#) consider seasonal daily maxima or Rx1Day, while here we consider pentad maxima. Furthermore, note that the year index represents a “season year” such that, for example, the 1950 DJF is defined as December, 1949 to February, 1950. While

Model	Label	Resolution	Ensemble members	CONUS grid cells
ECMWF-IFS-HR	ECMWF	$\approx 0.5^\circ$	4	3253
HadGEM3-GC31-HM	HadGEM	$\approx 0.25^\circ$	3	9900
IPSL-CM6A-ATM-HR	IPSL	$\approx 0.5^\circ$	1	2316
MPI-ESM1-2-XR	MPI	$\approx 0.5^\circ$	1	3748
CNRM-CM6-1-HR [†]	CNRM	$\approx 0.5^\circ$	1	3256

Table 1: Climate model output used in the analyses for this paper. [†]Note: the CNRM runs are only from 1981-2014.

the analysis described in Section 3 could be applied to all seasons, as mentioned in Section 1 we focus on the Boreal winter (DJF) as one might expect better agreement between models and observations in regions and/or seasons where parameterized convection processes are not a major factor.

2.2 Gridded daily data products

In order to compare results using the [Risser et al. \(2019b\)](#) methodology on GHCN station data with what might more traditionally be explored, we utilize the Livneh gridded data product ([Livneh et al., 2014](#)). This product consists of gridded daily precipitation data, and is derived from the same underlying GHCN data as described in Section 2.1. The Livneh product is available for 1950 to 2011; we regrid the raw data product to a regular $0.25^\circ \times 0.25^\circ$ grid to facilitate comparison with the climate model output described in Section 2.3. Similar to the GHCN data, here we extract the DJF Rx5Day for the Livneh product, defined as

$$\{Y_t^L(\mathbf{s}) : t = 1950, \dots, 2011; \mathbf{s} \in \mathcal{G}_L\},$$

where now \mathcal{G}_L is the $0.25^\circ \times 0.25^\circ$ grid over CONUS (with 12728 cells) and again we focus on DJF.

2.3 Climate models

As this study is motivated by the evaluation of high-resolution climate models, we utilize early submissions to the highresSST-present experiment of the HighResMIP subproject of the CMIP6 experiment ([Haarsma et al., 2016](#)), all of which are AMIP-style runs with fixed sea surface temperatures from 1950-2014.

- ECMWF-IFS-HR: The Integrated Forecasting System (IFS) model of the European Centre for Medium-range Weather Forecasting as configured for multi-decadal ensemble climate change experiments [Roberts et al. \(2018\)](#). Data is interpolated onto a 0.5×0.5 reg-

ular latitude-longitude grid from the native Tco399 cubic octahedral reduced Gaussian grid (nominally $\sim 25\text{km}$). The model has 91 vertical levels with the top model level at 1 hPa.

- HadGEM3-GC31-HM: The UK MetOffice Hadley Centre (Exeter, United Kingdom) unified climate model, HadGEM3-GC3.1-HM on a regular 768×1024 latitude-longitude grid (nominally 25km; [Roberts et al., 2019](#)) The model has 85 vertical levels with the top model level at 85 km.
- CNRM-CM6-1-HR: This model is developed jointly by the CNRM-GAME (Centre National de Recherches Météorologiques–Groupe d’études de l’Atmosphère Météorologique) in Toulouse, France and CERFACS (Centre Européen de Recherche et de Formation Avancée); see [Voldoire et al. \(2013\)](#). Data is interpolated to 0.5° regular latitude longitude grid from the native T3591 reduced Gaussian grid. The model has 91 vertical levels with the top level at 78.4km.
- MPI-ESM1-2-XR: The MPI-ESM1-2-XR from the Max Planck Institute for Meteorology in Hamburg, Germany ([Gutjahr et al., 2019](#)). Data is interpolated to a regular 768×384 longitude/latitude (nominally $\sim 50\text{km}$) from the native T255 spectral grid. The model has 95 vertical levels with the top model level at 0.1hPa.
- IPSL-CM6A-ATM-HR: This model is developed by the Institut Pierre Simon Laplace in Paris, France ([Boucher et al., 2019](#)). Data is interpolated from the native N256 geodesic grid to a 512×360 longitude-latitude grid. The model has 79 vertical levels with the top model level at 40000 m.

For each of these models (additional details provided in Table 1) and each ensemble member, we calculate the corresponding DJF Rx5Day values for each ensemble member in each grid box over CONUS. Furthermore, note that we mask out grid cells that are not fully over land. These values are denoted

$$\{Y_{t,e}^m(\mathbf{s}_i) : t = 1950, \dots, 2014; \mathbf{s} \in \mathcal{G}_m; e = 1, \dots, N_{\text{ens},m}\},$$

for model $m = 1, \dots, 5$, where \mathcal{G}_m is the model grid for model m and $N_{\text{ens},m}$ is the number of ensemble members for model m (see Table 1); however, note that the CNRM runs only cover 1981-2014.

3 Methods

3.1 Spatial extreme value analysis

The primary methodological tool used here is the spatial extreme value analysis outlined in [Risser et al. \(2019b\)](#), which is designed to characterize the spatially-complete climatological distribution of extreme precipitation based on measurements from irregularly observed weather stations. This analysis has two important features: first, it allows one to estimate the distribution of extreme precipitation even for locations where no data are available. Second, the methodology can be used for a large network of weather stations over a heterogeneous spatial domain like CONUS, which is critical for the problem at hand. However, the methodology can also be applied to climate model output by considering each grid cell measurement as a point measurement referenced at the center of the grid cell. And, in the case of model data, the underlying Gaussian process modeling provides a natural way to “regrid” the model data to a common grid using kriging, which is a data-driven gridding procedure that estimates the spatial length scale for smoothing; furthermore, in the Gaussian process methodology used here, the spatial length scale varies across the domain (i.e., we use a nonstationary covariance function).

For a full description of the methodology used, we refer the reader to [Risser et al. \(2019b\)](#). In short, the essence of the method is to first obtain estimates of the climatological features of extreme precipitation based on measurements from either the individual weather stations or the model grid cells via the Generalized Extreme Value (GEV) family of distributions, which is a modeling framework for the maxima of a process over a pre-specified time interval or “block,” e.g., the three-month DJF season used here. [Coles \(2001\)](#) (Theorem 3.1.1, page 48) shows that when the number of daily measurements is large (e.g., when considering the ≈ 90 daily measurements in a given season), the cumulative distribution function (CDF) of $Y_t(\mathbf{s})$ (which is the seasonal maximum daily precipitation measurement in year t at station \mathbf{s}) is a member of the GEV family

$$G_{\mathbf{s},t}(y) \equiv \mathbb{P}(Y_t(\mathbf{s}) \leq y) = \exp \left\{ - \left[1 + \xi_t(\mathbf{s}) \left(\frac{y - \mu_t(\mathbf{s})}{\sigma_t(\mathbf{s})} \right) \right]^{-1/\xi_t(\mathbf{s})} \right\}, \quad (1)$$

defined for $\{y : 1 + \xi_t(\mathbf{s})(y - \mu_t(\mathbf{s}))/\sigma_t(\mathbf{s}) > 0\}$. The GEV family of distributions (1) is characterized by three space-time parameters: the location parameter $\mu_t(\mathbf{s}) \in \mathcal{R}$, which describes the center of the distribution; the scale parameter $\sigma_t(\mathbf{s}) > 0$, which describes the spread of the distribution; and the shape parameter $\xi_t(\mathbf{s}) \in \mathcal{R}$. The shape parameter $\xi_t(\mathbf{s})$ is the most important for determining the qualitative behavior of the distribution of daily rainfall at a given location. If $\xi_t(\mathbf{s}) < 0$, the distribution has a finite upper bound; if $\xi_t(\mathbf{s}) > 0$, the distribution has no upper limit; and if $\xi_t(\mathbf{s}) = 0$, the distribution is again unbounded and the CDF (1) is interpreted as the limit $\xi_t(\mathbf{s}) \rightarrow 0$

(Coles, 2001). Note that Risser et al. (2019a) verify that the GEV approximation is appropriate for seasonal maxima (i.e., for a block size of 90) even if many of the seasonal measurements are zero, particularly when limiting oneself to return periods within the range of the data (as we consider here, with the 20-year return values).

While our goal is to simply estimate the climatology of extreme precipitation (and specifically not to estimate or detect trends), the nonstationarity of extreme precipitation over the last 70 years (see, e.g., Risser et al., 2019a) requires that we characterize a time-varying extreme value distribution. Here, we use the simple trend model

$$\mu_t(\mathbf{s}) = \mu_0(\mathbf{s}) + \mu_1(\mathbf{s})X_t, \quad \sigma_t(\mathbf{s}) \equiv \sigma(\mathbf{s}), \quad \xi_t(\mathbf{s}) \equiv \xi(\mathbf{s}), \quad (2)$$

where $X_t = [\log CO_2]_t$ is the natural logarithm of atmospheric carbon dioxide concentration in year t . The natural logarithm of atmospheric carbon dioxide concentration is a useful covariate for describing changes in the distribution of extreme precipitation (dating back to seminal work by Arrhenius, 1897, 1908); $\log CO_2$ has also been used elsewhere to characterize anthropogenic changes in extreme precipitation, e.g., Risser and Wehner (2017). While this is an admittedly simple temporal model, we argue that it is sufficient for characterizing the climatology of seasonal Rx5Day. Furthermore, Risser et al. (2019a) use a similar trend model as (2), which they show to be as good (in a statistical sense) as more sophisticated trend models (where, e.g., the scale and/or shape vary over time). We henceforth refer to $\mu_0(\mathbf{s})$, $\mu_1(\mathbf{s})$, $\sigma(\mathbf{s})$, and $\xi(\mathbf{s})$ as the *climatological coefficients* for location \mathbf{s} (weather station or model grid cell), as these values describe the climatological distribution of extreme precipitation in each year.

Conditional on station- or grid cell-specific estimates of the climatological coefficients, denoted

$$\{\tilde{\mu}_0(\mathbf{s}), \tilde{\mu}_1(\mathbf{s}), \tilde{\sigma}(\mathbf{s}), \tilde{\xi}(\mathbf{s}) : \mathbf{s} \in \mathcal{G}_{(\cdot)}\} \quad (3)$$

(where $\mathcal{G}_{(\cdot)}$ denotes the native grid cells or station locations), we next apply a spatial statistical approach using second-order nonstationary Gaussian processes to infer the underlying climatology over a fine grid via kriging. This approach yields fields of best estimates of the climatological coefficients, denoted

$$\{\hat{\mu}_0(\mathbf{s}), \hat{\mu}_1(\mathbf{s}), \hat{\sigma}(\mathbf{s}), \hat{\xi}(\mathbf{s}) : \mathbf{s} \in \mathcal{G}\}, \quad (4)$$

where \mathcal{G} is the 0.25° grid of $M = 13073$ grid cells over CONUS. These best estimates can be used to calculate corresponding estimates of the DJF r -year return value, denoted $\hat{\phi}_t^{(r)}(\mathbf{s})$, which is defined as the DJF maximum five-daily precipitation total that is expected to be exceeded on average once every r years. In other words, $\hat{\phi}_t^{(r)}(\mathbf{s})$ is an estimate of the $1 - 1/r$ quantile of the distribution of DJF maximum five-daily precipitation in year t at grid cell \mathbf{s} , i.e., $P(Y_t(\mathbf{s}) >$

$\widehat{\phi}_t^{(r)}(\mathbf{s}) = 1/r$, which can be written in closed form in terms of the climatological coefficients:

$$\widehat{\phi}_t^{(r)}(\mathbf{s}) = \begin{cases} [\widehat{\mu}_0(\mathbf{s}) + \widehat{\mu}_1(\mathbf{s})X_t] - \frac{\widehat{\sigma}(\mathbf{s})}{\widehat{\xi}(\mathbf{s})} [1 - \{-\log(1 - 1/r)\}^{-\widehat{\xi}(\mathbf{s})}], & \widehat{\xi}(\mathbf{s}) \neq 0 \\ [\widehat{\mu}_0(\mathbf{s}) + \widehat{\mu}_1(\mathbf{s})X_t] - \widehat{\sigma}(\mathbf{s}) \log\{-\log(1 - 1/r)\}, & \widehat{\xi}(\mathbf{s}) = 0 \end{cases} \quad (5)$$

(Coles, 2001). Note that $\widehat{\phi}_t^{(r)}(\mathbf{s}')$, the best estimate of the return value in year t , does not represent a return value estimated from a single year of data but is instead calculated using climatological coefficients estimated from the complete time record with the carbon dioxide concentration in year t (X_t in Eq. 5) plugged in. In other words, the time-varying return value estimates represent temporally smoothed quantities. Finally, note that we can similarly calculate return value estimates from the station- or grid cell-specific climatological coefficients from Eq. 3, denoted $\{\widehat{\phi}_t^{(r)}(\mathbf{s}) : \mathbf{s} \in \mathcal{G}_{(\cdot)}\}$.

3.2 Comparing the climatology of extreme precipitation

We illustrate the effect of geographic sampling and spatial statistics strategy on the evaluation of simulated 20-year return values of winter (DJF) maximum pentadal precipitation from selected high resolution climate models with two commonly used figures. Gleckler performance portraits (Gleckler et al., 2008) are used to show the model absolute and percentage bias (i.e., simulations minus observations) averaged over a region. Taylor diagrams (Taylor, 2001) plot the centered pattern correlation between observations and simulations as the angular dimension and the ratio of the observed to simulated spatial standard deviation as the radial dimension. These latter diagrams provide information about the spatial pattern of model errors with the biases removed. We choose 2014 as the reference year (i.e., we compare $\widehat{\phi}_{2014}^{(20)}(\mathbf{s})$), but note from Eq. 5 that this represents a temporally smoothed quantity and specifically not the return value estimated for a single year. The bias in 20-year return values (hereafter referred to as “extreme bias”) shown in the Gleckler performance portraits provides a simple measure of whether the models are too dry or too wet, while the Taylor diagram provides three useful metrics displayed in a single plot: (1) the spatial pattern correlation between the model and observations, (2) a comparison of the standard deviations, and (3) a skill score to assess the level of agreement between the two spatial fields. Taylor’s modified skill score \mathcal{S} , comparing two spatial fields (e.g., a model versus observations), is defined as

$$\mathcal{S} = \exp \left\{ -\frac{s_1^2 + s_2^2 - 2s_1s_2r}{2s_1s_2} \right\},$$

where s_j is the standard deviation of spatial field $j = 1, 2$ and r is the pointwise correlation between the two fields (also used in Wehner, 2013). The skill score essentially involves the ratio

of the mean squared error between the two fields (after removing the average from each field) and the standard deviations of each field; the score S ranges between 0 (indicating low skill) and 1 (indicating perfect skill). Further details on the Taylor diagrams are provided in Section 4; however, an important detail is that to calculate a Taylor diagram we must have “paired” observations and model data, i.e., both data sources must be defined on the same spatial support or grid.

In order to illustrate the effect of geographic sampling, we can compare the Gleckler and Taylor diagrams for three approaches:

C1 Traditional approach: what might typically be done without regard for the geographic sampling bias, using daily gridded products (i.e., without spatial statistics and kriging/re-gridding)

Comparison C1 is designed to reflect what a traditional analysis might set out to compare, wherein the return values are calculated independently for each model grid cell (i.e., based on the climatological coefficients in Eq. 3); see, e.g., Wehner (2013). Then, in order to estimate a spatially-complete extreme climatology, a similar analysis is applied to the Livneh data product, again estimating return values separately for each Livneh grid cell. Finally, we re-grid the model return values to live on the Livneh grid using bilinear interpolation.

C2 Accounting for geographic sampling bias

However, comparison C1 ignores the fact that a climate model yields spatially-complete information, while any observational data product is only representative of the underlying weather stations, which of course are irregularly spaced over CONUS and are much more spatially dense in some parts of CONUS (e.g., Kansas) than others (e.g., Utah or Nevada); see Figure A.1. To more appropriately compare the model with the GHCN station data, we can compare the extreme climatology for a subset of the model grid cells. Here, we first overlay the GHCN station locations onto the model grid and choose the grid cell closest to each GHCN station. We also spatially sub-sample the GHCN station locations by subsequently choosing the GHCN station closest to each model grid cell center. (See Figure A.1 for the subsampled grid cells and stations.) This procedure ensures that we have the same amount of data (spatially) from both the weather stations and the climate model, in that the number of grid cells now matches the number of stations. Using these subsampled data sets, as in C1 we can compare the return values for model versus GHCN stations, where again the return values are calculated independently for each grid cell or station (again using the climatological coefficients in Eq. 3), *without* the spatial statistical modeling and kriging. The Taylor diagram is calculated based on the “matched” pairs of grid cells and stations.

C3 Account for the geographic sampling bias and utilizing spatial statistics with kriging/re-gridding

Finally, we can both account for the geographic sampling bias and utilize the methodology of [Risser et al. \(2019b\)](#) to borrow strength spatially and use data-driven kriging to re-grid the return values to a common grid for both the models and observations. As mentioned in Section 3.1, we use kriging to map all return values onto the same $0.25^\circ \times 0.25^\circ$ grid over CONUS; for the Taylor diagram, it is now straightforward to consider pairs of grid cells. Specifically, for this final comparison, we use the same input data as in C2 (subsampled stations and subsampled model grid cells), but use kriging to put both data sets on a common grid.

We argue that C1 is the “wrong” comparison, in that it uses a suboptimal comparison data set (a daily gridded product, which is biased for evaluating extremes) and furthermore ignores the geographic sampling bias. Comparison C2 is an improvement on C1 in that it accounts for geographic sampling by using model data in a manner geographically consistent with available station data; finally, C3 is the “right” comparison because it uses a comparable amount of information, the correct data source (i.e., in situ measurements), and borrows strength spatially via data-driven kriging.

Note that these comparisons are not exhaustive: we could also compare a spatial analysis of the Livneh data, or sub-sample Livneh according to the geographic distribution of the in situ measurements (as in C2). However, given that one of our main points is that a daily gridded product like Livneh is a suboptimal data source for evaluating extremes, we limit our focus to the aforementioned comparisons.

4 Results

For reference, we have provided two supplemental figures that summarize the 20-year return value estimates for each model and data product. First, Figure A.2 in the Appendix shows the estimated DJF 20-year return values for Rx5Day for Livneh and the five models, where the estimates are calculated separately for each grid cell and shown on the native grid (i.e., these are the estimates involved in comparison C1). Second, Figure A.3 in the Appendix shows the gridded estimates of 20-year return values from the GHCN station data using the [Risser et al. \(2019b\)](#) methodology (panel a.); panels b. and c. show the absolute difference and percent difference, respectively, between the GHCN estimates and the estimates obtained from the [Livneh et al. \(2014\)](#) data product and models. The Livneh comparison is based on the estimates shown in Figure A.2; otherwise, the model comparisons use the estimates calculated from the subsampled model data using the [Risser et al. \(2019b\)](#) methodology to do spatial smoothing and gridding/kriging (i.e., these are the estimates involved in comparison C3).

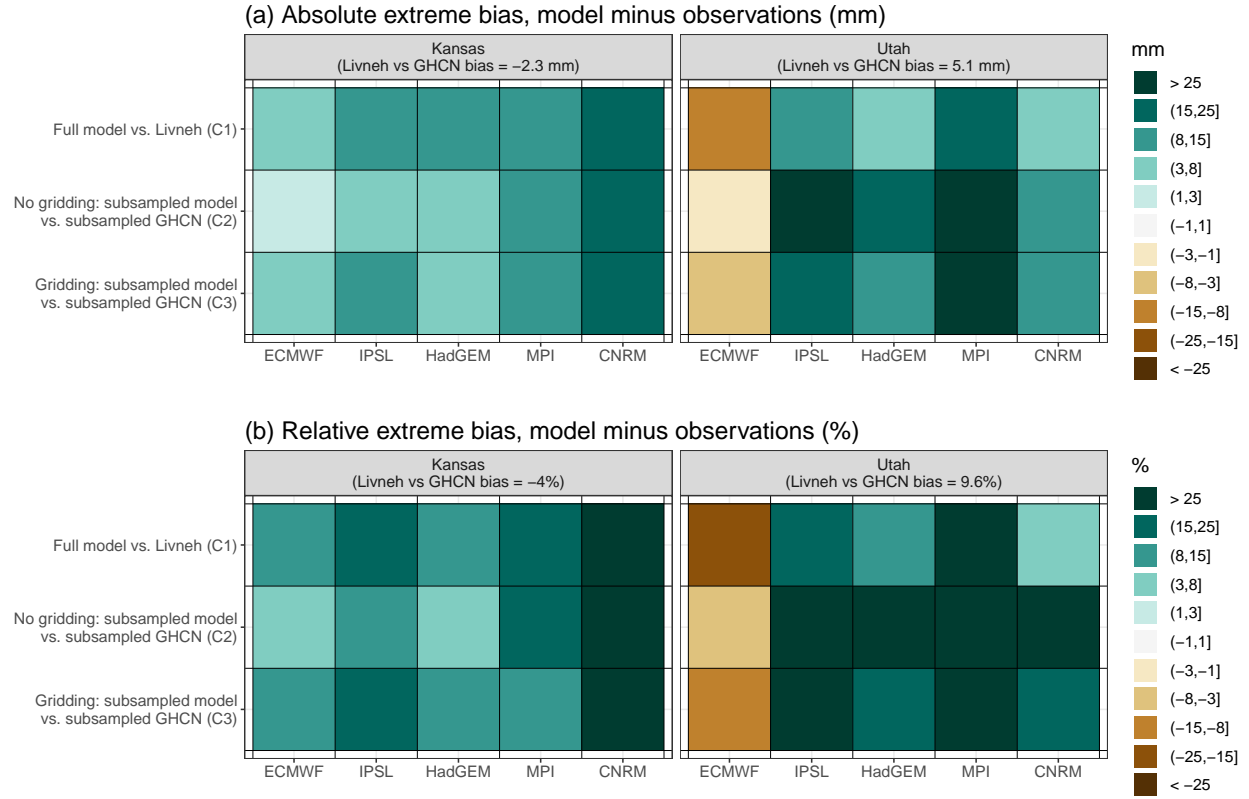


Figure 1: Gleckler performance portraits showing extreme bias, both absolute (in mm; panel a) and relative (in %; panel b), averaged for the six models over Kansas and Utah, across comparisons C1, C2, and C3. The Livneh vs. GHCN bias compares the extreme climatology calculated from Livneh et al. (2014) and the probabilistic gridded product of Risser et al. (2019b).

4.1 Case study: Kansas versus Utah

To illustrate the methodology and evaluate comparisons C1, C2, and C3, we first explore return value estimates for two small spatial subregions that exhibit very different sampling by the GHCN network, namely Kansas and Utah. These two states present a illustrative case study for our method because Utah is poorly sampled, while Kansas is well sampled. Also, while the orographic characteristics of these regions are very different, the overall climatology is roughly similar for DJF precipitation.

First, the extreme bias averaged over each of these regions is shown in Figure 1 (also shown in Table A.2 in the Appendix), showing both relative (i.e., percent) and absolute (i.e., millimeters) bias. The biases are calculated using the values plotted in Figure A.2 (after regridding, for C1) and Figure A.3 (for C3). Note that relative to a data set based on the methodology of Risser et al. (2019b), the Livneh product has a slight dry bias (-2.3mm or -4%) for Kansas but a slight

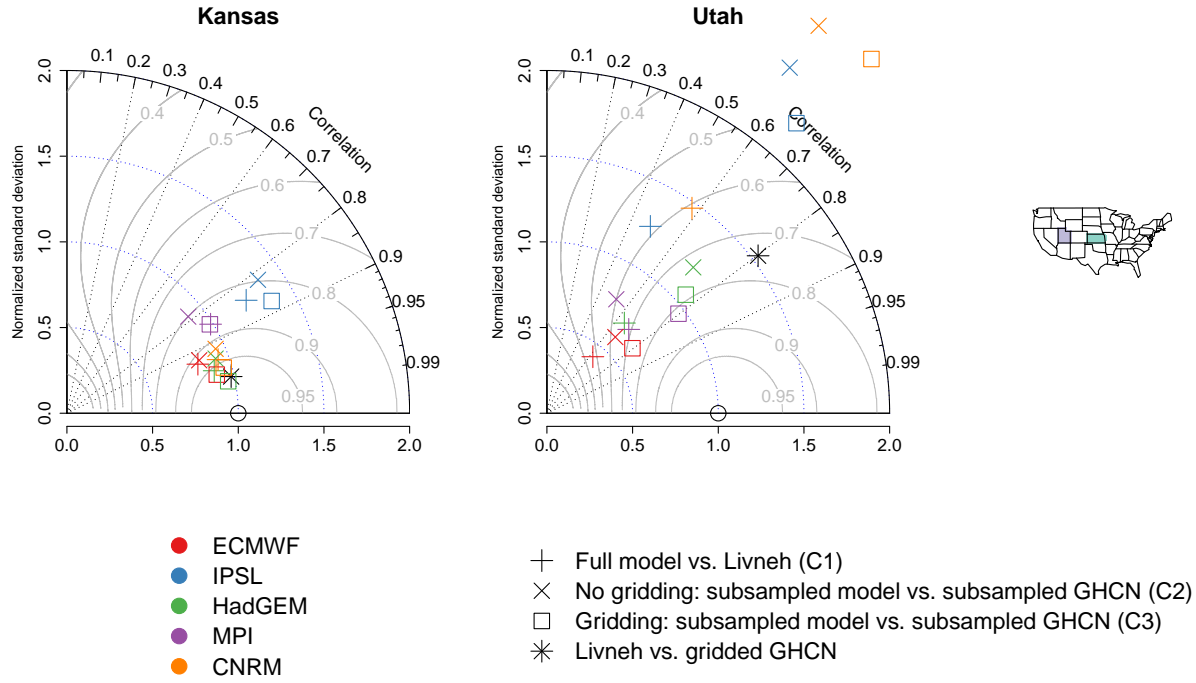


Figure 2: Taylor diagrams comparing 20-year return values for Utah and Kansas across five climate models. The “+” symbol corresponds to C1; the \times symbol corresponds to C2; the square symbol corresponds to C3. Finally, the star symbol serves as a reference for Livneh versus the gridded product of [Risser et al. \(2019b\)](#). The gray curvilinear lines represent the skill score for each model relative to the reference data set.

wet bias in Utah (5.1mm or 9%); the dry bias in Kansas is expected given the fractal scaling properties of daily precipitation, while the wet bias in Utah is likely due to orographic adjustments in Livneh (note that the [Risser et al., 2019b](#) analysis includes an orographic adjustment, but this is estimated directly from the weather station data and does not explicitly incorporate physical forcing relationships). Considering the climate models, all models exhibit a wet bias in extremes for Kansas regardless of the comparison; furthermore, the bias appears to be roughly the same regardless of the comparison method—even for C1, which uses the “wrong” data source. However, things are quite different for Utah: first of all, the model biases vary greatly across the different climate models (ranging from +3% to over +25%), and ECMWF even has a dry bias. Furthermore, comparison C1 implies a false confidence in the models, in that the extreme bias is much worse when accounting for geographic sampling in C2 (except for ECMWF). Another interesting point is that for Utah, the C3 comparison that incorporates data-driven gridding improves the bias relative to C2; furthermore, C3 provides a compromise between the artificial confidence in the models relative to Livneh and the adjusted bias of the C2 comparison.

The Taylor diagrams comparing 20-year return values for Kansas and Utah are shown in Figure 2. Clearly, as with the bias, the performance of the various climate models in replicating the pattern of extreme precipitation is very different for these two states. Despite the small area of these regions, the models (and even the Livneh observations) are uniformly better in Kansas (where the geographic sampling is quite dense) than in Utah (where the geographic sampling is sparse and irregular). In both states (and similar to the extreme bias comparison), the + symbol (comparison C1) implies a false overconfidence in the model, as evidenced by the fact that the × symbol (comparison C2) is usually worse. However, the square symbol (comparison C3) presents an improvement over the × comparison—again as was seen for the extreme bias. The relative differences between these three comparisons are very different for Utah relative to Kansas: the distance between comparisons C1 (+) and C2 (×) are much larger for Utah. On the other hand, the relative ordering is the same in both states. Finally, the Taylor diagrams imply a ranking of the models’ quality in simulating the pattern of extreme precipitation despite the fairly small number of grid points in these 2 regions. The HadGEM model looks relatively good in both regions; MPI is somewhat good for both regions; IPSL performs poorly in both regions; CNRM is performs well in Kansas but very poorly in Utah.

In summary, the main points of this case study are as follows: for well-sampled regions (like Kansas), the extreme bias, spatial pattern correlation, and spatial variability are approximately the same regardless of whether geographic sampling is explicitly accounted for, while for poorly sampled regions (like Utah) a traditional comparison versus Livneh implies an overconfidence in the models. For a well-sampled region, an appropriate comparison (C3) improves the model skill scores relative to a traditional (inappropriate) comparison; for a poorly-sampled region, the implied change to model skill is less clear. While there are important inter-model differences, note that these differences are smaller for a well-sampled region than for a poorly-sampled region. Note that we do not argue that comparison C3 makes the models look better or worse (indeed both situations occur for this case study); instead, it gives a more appropriate sense of the models’ performance.

4.2 Comparisons for CONUS and large climate subregions

To explore these considerations more broadly, we now expand the scope of our model evaluation to systematically consider all of CONUS and seven spatial subregions. These subregions (shown in Figure 4 and also with labels in Figure A.4 in the Appendix) are loosely based upon the climate regions used in the National Climate Assessment (Wuebbles et al., 2017), with a small adjustment in the western United States to make the regions somewhat homogeneous with respect to the geographic sampling of the GHCN stations. Table A.1 in the Appendix summarizes the number of

0.25° grid cells and original GHCN stations in each subregion. The Taylor diagram skill scores and extreme biases (absolute and relative) for CONUS and the subregions are shown in Tables A.3 and A.4 in the Appendix.

First considering the extreme bias in Figure 3, note that while the models are mostly too wet across all regions, there are some models and regions that display a dry bias. As in Section 4.1, the biases are calculated using the values plotted in Figure A.2 (after regridding, for C1) and Figure A.3 (for C3). In general the models are very noisy, e.g., ECMWF is generally too dry but has a wet bias in the Northern Great Plains; also, the extreme bias for the Pacific Coast across models is either much too dry or much too wet. For CONUS we can see that most models have a wet bias in the extremes overall, with ECMWF being the lone exception. When considering a large spatial average like CONUS, the extreme bias is roughly the same across comparisons C1, C2, and C3, although there is some improvement for C2 and C3 relative to C1, at least for IPSL, HadGEM, MPI, and CNRM. When considering the climate subregions, in the Southeast a majority of the models now display a dry bias in extremes, and for this region there are major differences in the bias when accounting for geographic sampling. However, in some cases this adjustment improves the bias (HadGEM and IPSL) while in others the adjustment makes the bias worse (ECMWF, MPI, and CNRM). As was seen in Section 4.1, regions with dense geographic sampling (Midwest and Southern Great Plains, which have almost one station for every two 0.25° grid cells) have minimal extreme bias (particularly in a relative sense) across models, although accounting for geographic sampling (C2) and gridding (C3) improves the bias for most models. For a poorly-sampled region like the Mountain West (with only about one station per every four 0.25° grid cells), comparison C1 again tends to imply a false confidence in the models' ability to characterize extremes: the bias for C2 is uniformly worse across models.

Now considering the Taylor Diagrams in Figure 4, the effect of geographic sampling is minimal when considering very large averages (like CONUS) and regions with dense geographic sampling (like the Southeast, Southern Great Plains, and the Midwest with approximately one station for every two 0.25° grid cells): for these areas the difference between a traditional comparison (C1, the + symbol) and explicitly accounting for geographic sampling (\times and the square symbols) are relatively quite small. However, there are again important inter-model differences: for CONUS, the CNRM and IPSL models are generally over-dispersed (i.e., there is too much spatial variability) while ECMWF and MPI are underdispersed (i.e., too little spatial variability); furthermore, the spatial pattern correlations range from approximately 0.65 (IPSL) to 0.9 (HadGEM and MPI). However, as was seen in the case study, for regions with poor geographic sampling (like the Mountain West and Pacific Coast), failing to account for geographic sampling implies an overconfidence in the models: the + symbols (C1) are generally much better than the \times (C2) symbol in terms of spatial variability, pattern correlation, and the skill score. Once again, accounting for both the

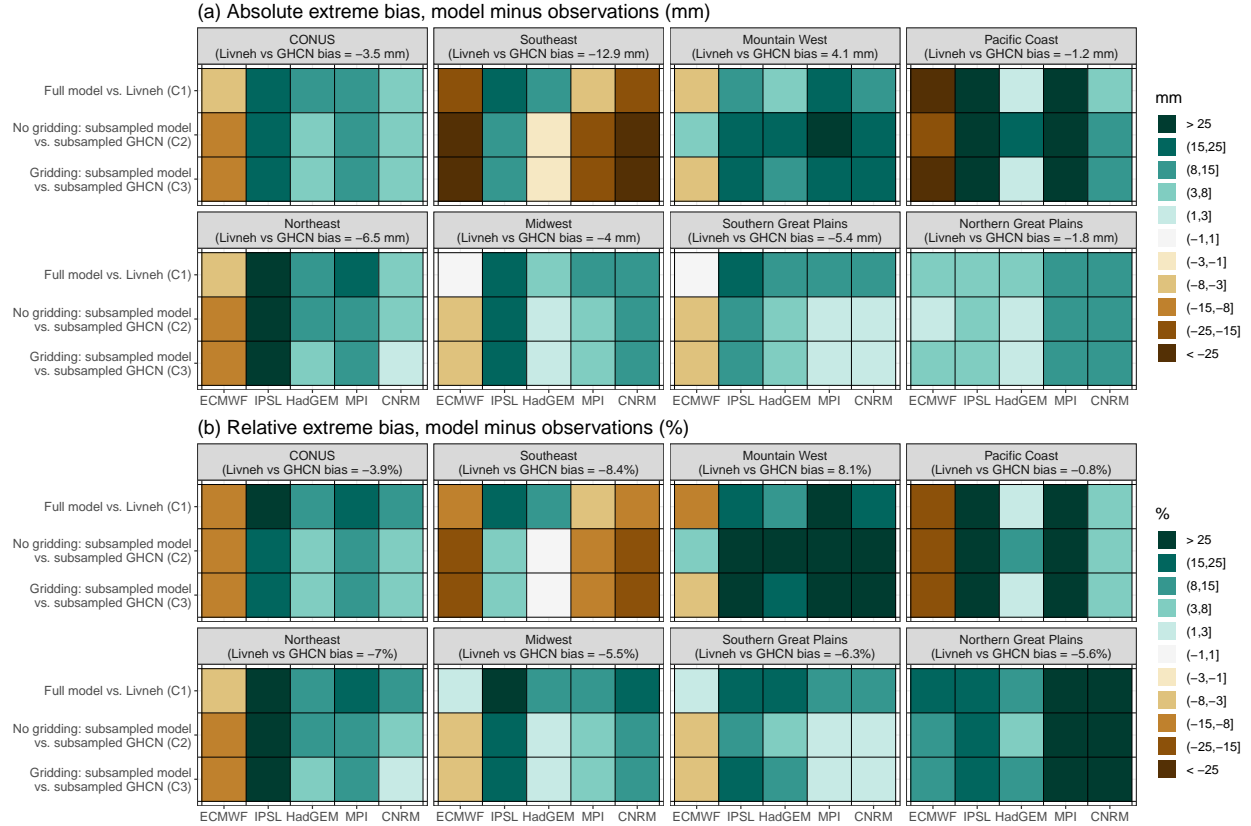


Figure 3: Gleckler performance portraits showing extreme bias, both absolute (in mm; panel a) and relative (in %; panel b), averaged for the five models over CONUS and the seven subregions shown in Figure A.4, across comparisons C1, C2, and C3. The Livneh vs. GHCN bias compares the extreme climatology calculated from Livneh et al. (2014) and the probabilistic gridded product of Risser et al. (2019b).

geographic sampling and borrowing strength spatially (C3) provides an improvement for all metrics shown in the Taylor diagram in these regions, relative to simply accounting for geographic sampling (C2). Looking at just the skill scores (shown in Tables A.3 and A.4 in the Appendix), for a well-sampled region like the Midwest the scores are consistently large (≥ 0.9) with little variability across the different models and even comparisons C1-C3 (note, however, that this is not the case for the bias, even for a well-sampled region). On the other hand, in the poorly-sampled Mountain West there are large differences in the skill scores across models, and furthermore the different comparisons C1-C3 are highly variable in their relative ordering. Interestingly, for the skill scores, comparison C3 yields almost uniformly larger skill scores than comparison C1 across all models and all regions (except for a few cases where the decrease is on the order of 0.02-0.05): in other words, a more appropriate comparison generally improves the skill of each model with respect to the variability and spatial pattern (although this is not the case for the bias).

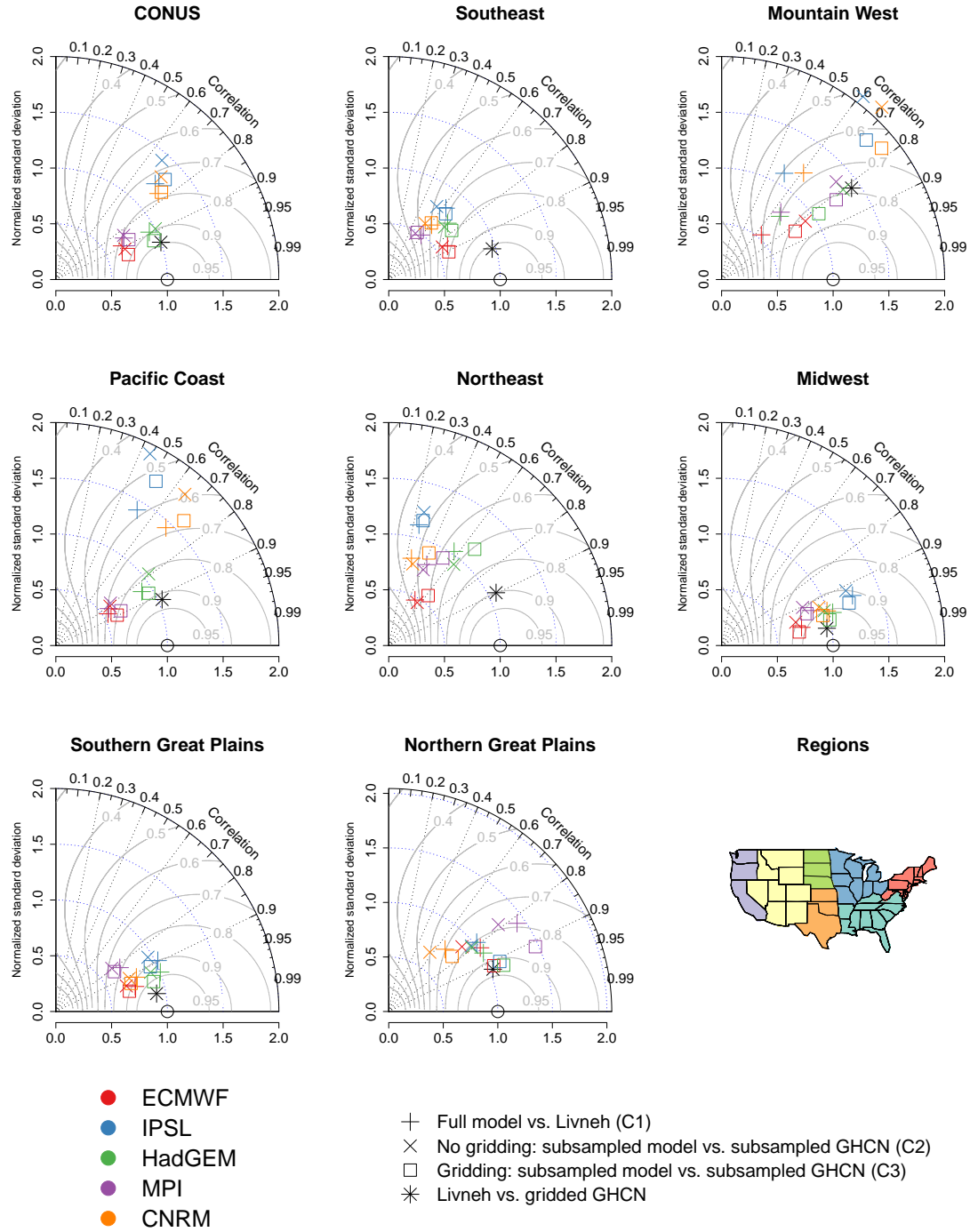


Figure 4: Taylor diagrams comparing 20-year return values for pentad maxima across CONUS and seven subregions, for five climate models. The “+” symbol corresponds to C1; the × symbol corresponds to C2; the square symbol corresponds to C3. Finally, the star symbol serves as a reference for Livneh versus the gridded product of [Risser et al. \(2019b\)](#). The gray curvilinear lines represent the skill score for each model relative to the reference data set.

In summary, as with the case study in Section 4.1, our main point is that the sampling methodology is more important for poorly sampled areas than for well-sampled areas. For well-sampled regions both the extreme bias and Taylor diagram are relatively similar whether or not geographic sampling is accounted for, although when considering bias the models can be either fairly consistent for these regions (e.g., the Southern Great Plains) or show extreme variability (e.g., the Southeast). For poorly sampled regions like the Mountain West, comparison with a gridded daily product implies an overconfidence in the models, but the spatial analysis provides a major improvement over only accounting for the geographic sampling. Note that while both the extreme bias and the Taylor diagrams imply a relative ranking of the models, there are some regions where the models’ performance is very similar across the five models (e.g., the Midwest and Southeast) and others where the models are all over the place (e.g., the Pacific Coast and Mountain West). Interesting, even for well-sampled regions with consistent model performance, the models can collectively perform either quite well (e.g., the Midwest) or very poorly (e.g., the Southeast).

5 Discussion

In this paper, we have highlighted two important issues in comparing extremes from climate model output with observational data: (1) the improper use of daily gridded products, and (2) failing to account for the geographic sampling of weather station data. Our analysis of extreme pentadal precipitation demonstrates that the choice of methodology for conducting model comparison (in terms of observational data set choice and accounting for sampling) is relatively unimportant for well-sampled domains but highly important for poorly sampled regions. We expect that these geographic sampling issues for extreme pentadal totals would also be relevant to extreme daily and subdaily precipitation and possibly the mean precipitation climatology. Note that we are not suggesting that the method for comparing models and observational data for extremes will make the models look either better or worse (indeed, each situation arises in our case studies); instead, we argue that using “raw” in situ measurements and accounting for the geographic sampling paints a more appropriate picture of the models’ performance. Finally, the integrated metrics considered in this paper (namely, extreme bias and Taylor diagrams) are helpful for gaining an overall sense of the models’ ability to characterize the extreme climatology, but at the end of the day the quality of the local performance at high resolutions may be much different than what is suggested by, e.g., a spatially-averaged bias.

While this paper does not specifically set out to conduct a full evaluation or ranking of the model data under consideration, the maps shown in Figure A.3 contain important information on the quality of the various models’ ability to characterize the observed extreme precipitation climatology over CONUS, as well as quantifying how the models relate to one another. For example,

in the eastern United States, the errors present in the HadGEM and IPSL models have a similar spatial pattern; ECMWF, MPI, and CNRM form a second “cluster” of error patterns. In the Rocky Mountains, all of the models except ECMWF are too wet, while the ECMWF runs are generally too dry. These differences are likely related to the models’ ability to simulate wintertime storms; further analysis (including the tracking of such storms) is beyond the scope of this paper. Finally, in the western coastal states, all models exhibit a dry bias right along the coast, which could be due to either errors in the models’ ability to characterize the climatology of atmospheric rivers or simply an artifact of the missing effects of orography in models with a horizontal resolution of $\approx 0.25^\circ$ to 0.5° . A formal model comparison study is reserved for future work.

It is important to note that our definitions of “well-sampled” and “poorly sampled” in this paper are all relative to the contiguous United States, which is extremely well sampled overall relative to many other land regions. Nonetheless, we have demonstrated the importance of accounting for geographic sampling, even for one of the most well-sampled parts of the globe. Sampling considerations will be even more important for the very poorly sampled parts of the world, for example, Africa, South America, and northern Asia. We hypothesize that the differences between the various comparisons C1, C2, and C3 would be even larger for these regions.

Acknowledgements

The observational data supporting this article are based on publicly available measurements from the National Centers for Environmental Information (<ftp://ftp.ncdc.noaa.gov/pub/data/ghcn/daily/>). Model data was obtained for the IPSL and CNRM models from the Earth System Grid (<https://esgf-node.llnl.gov/search/cmip6/>) and for the other models by early access to the Jasmin server in the UK. It is expected that all data used in this paper will eventually be uploaded to the CMIP6 data portals by the modeling groups themselves.

This research was supported by the Director, Office of Science, Office of Biological and Environmental Research of the U.S. Department of Energy under Contract No. DE-AC02-05CH11231 and used resources of the National Energy Research Scientific Computing Center (NERSC), also supported by the Office of Science of the U.S. Department of Energy, under Contract No. DE-AC02-05CH11231.

This document was prepared as an account of work sponsored by the United States Government. While this document is believed to contain correct information, neither the United States Government nor any agency thereof, nor the Regents of the University of California, nor any of their employees, makes any warranty, express or implied, or assumes any legal responsibility for the accuracy, completeness, or usefulness of any information, apparatus, product, or process disclosed, or represents that its use would not infringe privately owned rights. Reference herein to

any specific commercial product, process, or service by its trade name, trademark, manufacturer, or otherwise, does not necessarily constitute or imply its endorsement, recommendation, or favoring by the United States Government or any agency thereof, or the Regents of the University of California. The views and opinions of authors expressed herein do not necessarily state or reflect those of the United States Government or any agency thereof or the Regents of the University of California.

References

- Arrhenius, S. (1897). On the influence of carbonic acid in the air upon the temperature of the Earth. *Publications of the Astronomical Society of the Pacific*, 9:14.
- Arrhenius, S. (1908). *Worlds in the making: the evolution of the universe*. Harper & Brothers.
- Boucher, O., Denvil, S., Caubel, A., and Foujols, M. A. (2019). IPSL IPSL-CM6A-ATM-HR model output prepared for CMIP6 HighResMIP.
- Coles, S. (2001). *An Introduction to Statistical Modeling of Extreme Values*. Lecture Notes in Control and Information Sciences. Springer.
- Gervais, M., Tremblay, L. B., Gyakum, J. R., and Atallah, E. (2014). Representing extremes in a daily gridded precipitation analysis over the United States: Impacts of station density, resolution, and gridding methods. *Journal of Climate*, 27(14):5201–5218.
- Gleckler, P. J., Taylor, K. E., and Doutriaux, C. (2008). Performance metrics for climate models. *Journal of Geophysical Research: Atmospheres*, 113(D6).
- Gutjahr, O., Putrasahan, D., Lohmann, K., Jungclaus, J. H., von Storch, J. S., Brüggemann, N., Haak, H., and Stoessel, A. (2019). Max Planck Institute Earth System Model (MPI-ESM1. 2) for High-Resolution Model Intercomparison Project (HighResMIP). *Geophysical Model Development*, 12:3241–3281.
- Haarsma, R. J., Roberts, M. J., Vidale, P. L., Senior, C. A., Bellucci, A., Bao, Q., Chang, P., Corti, S., Fučkar, N. S., Guemas, V., et al. (2016). High resolution model intercomparison project (HighResMIP v1. 0) for CMIP6. *Geoscientific Model Development*, 9(11):4185–4208.
- Jones, P., Osborn, T., Briffa, K., Folland, C., Horton, E., Alexander, L., Parker, D., and Rayner, N. (2001). Adjusting for sampling density in grid box land and ocean surface temperature time series. *Journal of Geophysical Research: Atmospheres*, 106(D4):3371–3380.
- King, A. D., Alexander, L. V., and Donat, M. G. (2013). The efficacy of using gridded data to examine extreme rainfall characteristics: a case study for Australia. *International Journal of Climatology*, 33(10):2376–2387.
- Livneh, B., Rosenberg, E. A., Lin, C., Nijssen, B., Mishra, V., Andreadis, K. M., Maurer, E. P., and Lettenmaier, D. P. (2014). A long-term hydrologically based dataset of land surface fluxes

- and states for the conterminous United States: Update and extensions. *Journal of Climate*, 27(1):478.
- Lovejoy, S., Schertzer, D., and Allaire, V. (2008). The remarkable wide range spatial scaling of TRMM precipitation. *Atmospheric Research*, 90(1):10–32.
- Madden, R. A. and Meehl, G. A. (1993). Bias in the global mean temperature estimated from sampling a greenhouse warming pattern with the current surface observing network. *Journal of Climate*, 6(12):2486–2489.
- Maskey, M. L., Puente, C. E., Sivakumar, B., and Cortis, A. (2016). Encoding daily rainfall records via adaptations of the fractal multifractal method. *Stochastic Environmental Research and Risk Assessment*, 30(7):1917–1931.
- Menne, M. J., Durre, I., Vose, R. S., Gleason, B. E., and Houston, T. G. (2012). An overview of the Global Historical Climatology Network-Daily database. *Journal of Atmospheric and Oceanic Technology*, 29(7):897–910.
- Risser, M. D., Paciorek, C. J., O’Brien, T. A., Wehner, M. F., and Collins, W. D. (2019a). Detected changes in precipitation extremes at their native scales derived from in situ measurements. *Journal of Climate*, 32(23):8087–8109.
- Risser, M. D., Paciorek, C. J., Wehner, M. F., O’Brien, T. A., and Collins, W. D. (2019b). A probabilistic gridded product for daily precipitation extremes over the United States. *Climate Dynamics*, 53(5):2517–2538.
- Risser, M. D. and Wehner, M. F. (2017). Attributable human-induced changes in the likelihood and magnitude of the observed extreme precipitation during Hurricane Harvey. *Geophysical Research Letters*, 44(24):12,457–12,464.
- Roberts, C. D., Senan, R., Molteni, F., Boussetta, S., Mayer, M., and Keeley, S. P. (2018). Climate model configurations of the ECMWF Integrated Forecasting System (ECMWF-IFS cycle 43r1) for HighResMIP. *Geoscientific Model Development*, 11(9):3681–3712.
- Roberts, M. J., Baker, A., Blockley, E. W., Calvert, D., Coward, A., Hewitt, H. T., Jackson, L. C., Kuhlbrodt, T., Mathiot, P., Roberts, C. D., Schiemann, R., Seddon, J., Vannière, B., and Vidale, P. L. (2019). Description of the resolution hierarchy of the global coupled HadGEM3-GC3.1 model as used in CMIP6 HighResMIP experiments. *Geoscientific Model Development Discussions*, 2019:1–47.
- Taylor, K. E. (2001). Summarizing multiple aspects of model performance in a single diagram. *Journal of Geophysical Research: Atmospheres*, 106(D7):7183–7192.
- Thornton, P. E., Thornton, M. M., Mayer, B. W., Wilhelmi, N., Wei, Y., Devarakonda, R., and Cook, R. B. (2014). Daymet: Daily Surface Weather Data on a 1-km Grid for North America, Version 2. Technical report, Oak Ridge National Lab (ORNL), Oak Ridge, TN (United States).

- Timmermans, B., Wehner, M., Cooley, D., O'Brien, T., and Krishnan, H. (2019). An evaluation of the consistency of extremes in gridded precipitation data sets. *Climate Dynamics*, 52(11):6651–6670.
- Voldoire, A., Sanchez-Gomez, E., Salas y Mélia, D., Decharme, B., Cassou, C., Sénési, S., Valcke, S., Beau, I., Alias, A., Chevallier, M., Déqué, M., Deshayes, J., Douville, H., Fernandez, E., Madec, G., Maisonnave, E., Moine, M.-P., Planton, S., Saint-Martin, D., Szopa, S., Tyteca, S., Alkama, R., Belamari, S., Braun, A., Coquart, L., and Chauvin, F. (2013). The CNRM-CM5.1 global climate model: description and basic evaluation. *Climate Dynamics*, 40(9):2091–2121.
- Vose, R. S., Wuertz, D., Peterson, T. C., and Jones, P. (2005). An intercomparison of trends in surface air temperature analyses at the global, hemispheric, and grid-box scale. *Geophysical Research Letters*, 32(18).
- Wehner, M. F. (2013). Very extreme seasonal precipitation in the NARCCAP ensemble: model performance and projections. *Climate Dynamics*, 40(1-2):59–80.
- Wuebbles, D. J., Fahey, D. W., and Hibbard, K. A. (2017). Climate science special report: fourth National Climate Assessment, volume I.

A Supplemental figures

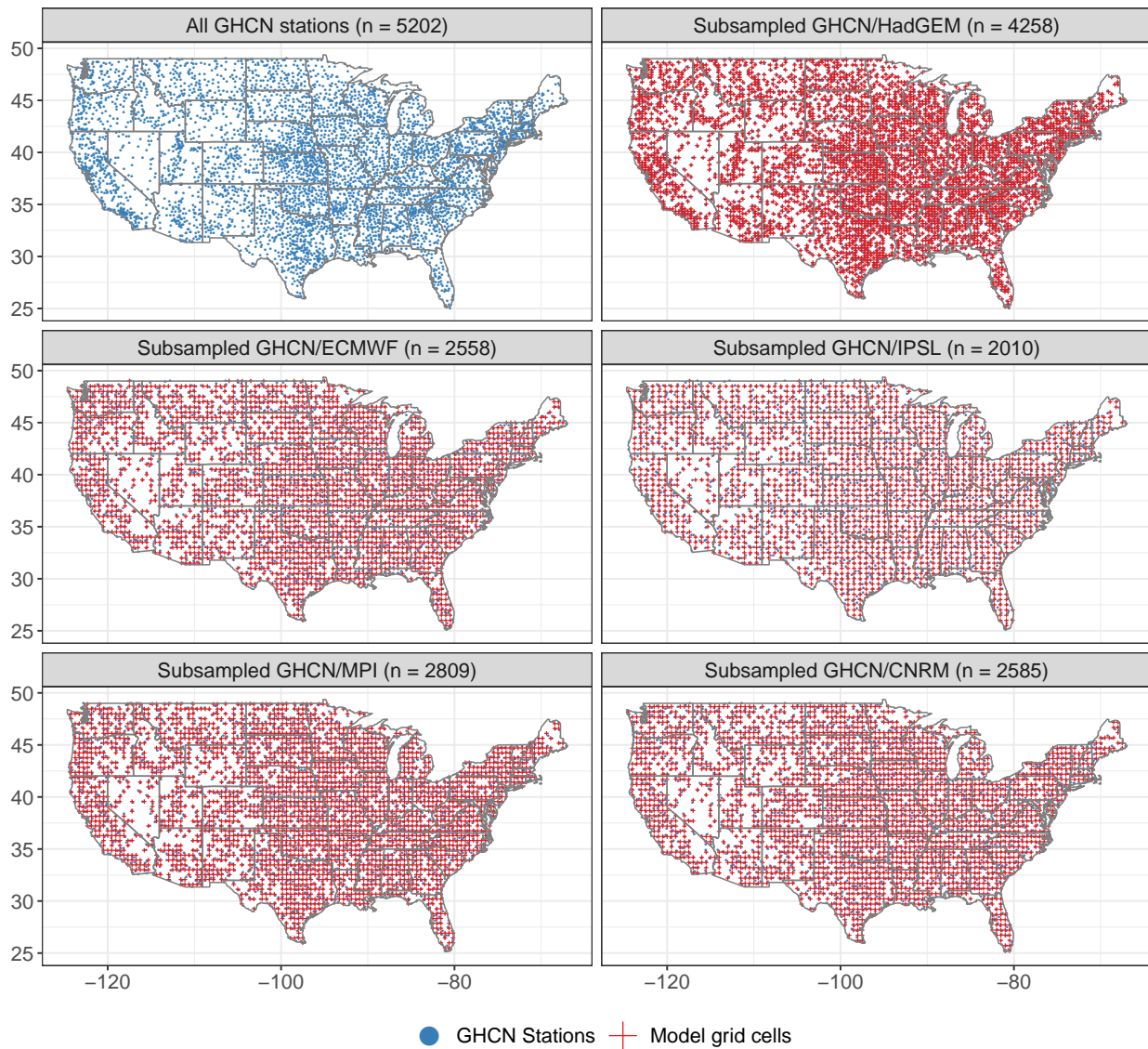


Figure A.1: The spatial distribution of the $n = 5202$ GHCN stations with a minimum of 66.7% of daily precipitation measurements over December, 1949 to November, 2017 (top left). The other five panels show the subsampled and matched GHCN stations and model grid cells for HadGEM3 (top right; $n = 4258$), ECMWF (middle left; $n = 2558$), IPSL (middle right; $n = 2010$), MPI (middle left; $n = 2809$), and CNRM (middle right; $n = 2585$).

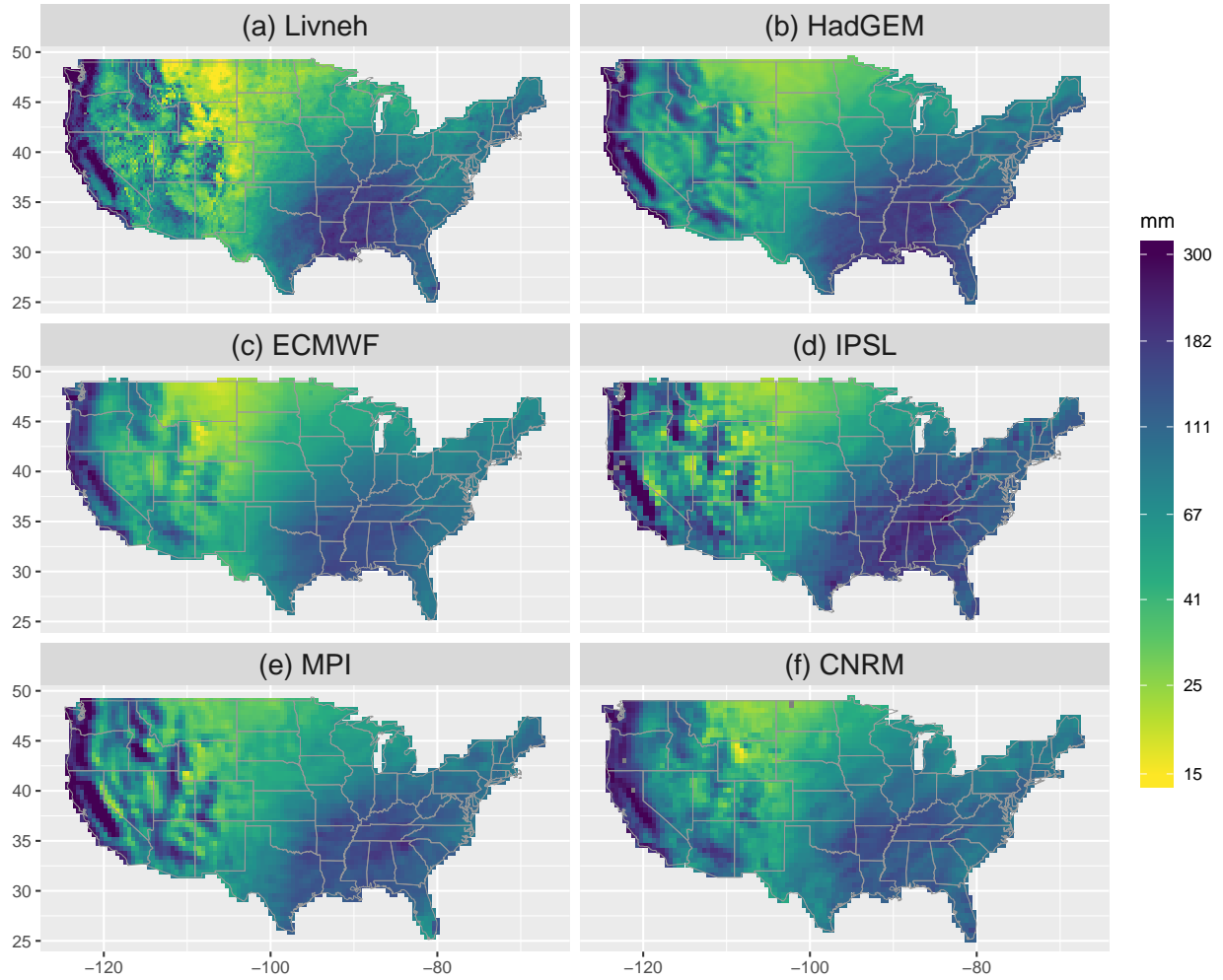


Figure A.2: Wintertime (DJF) 20-year return values in Rx5Day (mm) for each model and the [Livneh et al. \(2014\)](#) gridded product, calculated separately for each grid cell and shown on the native grid.

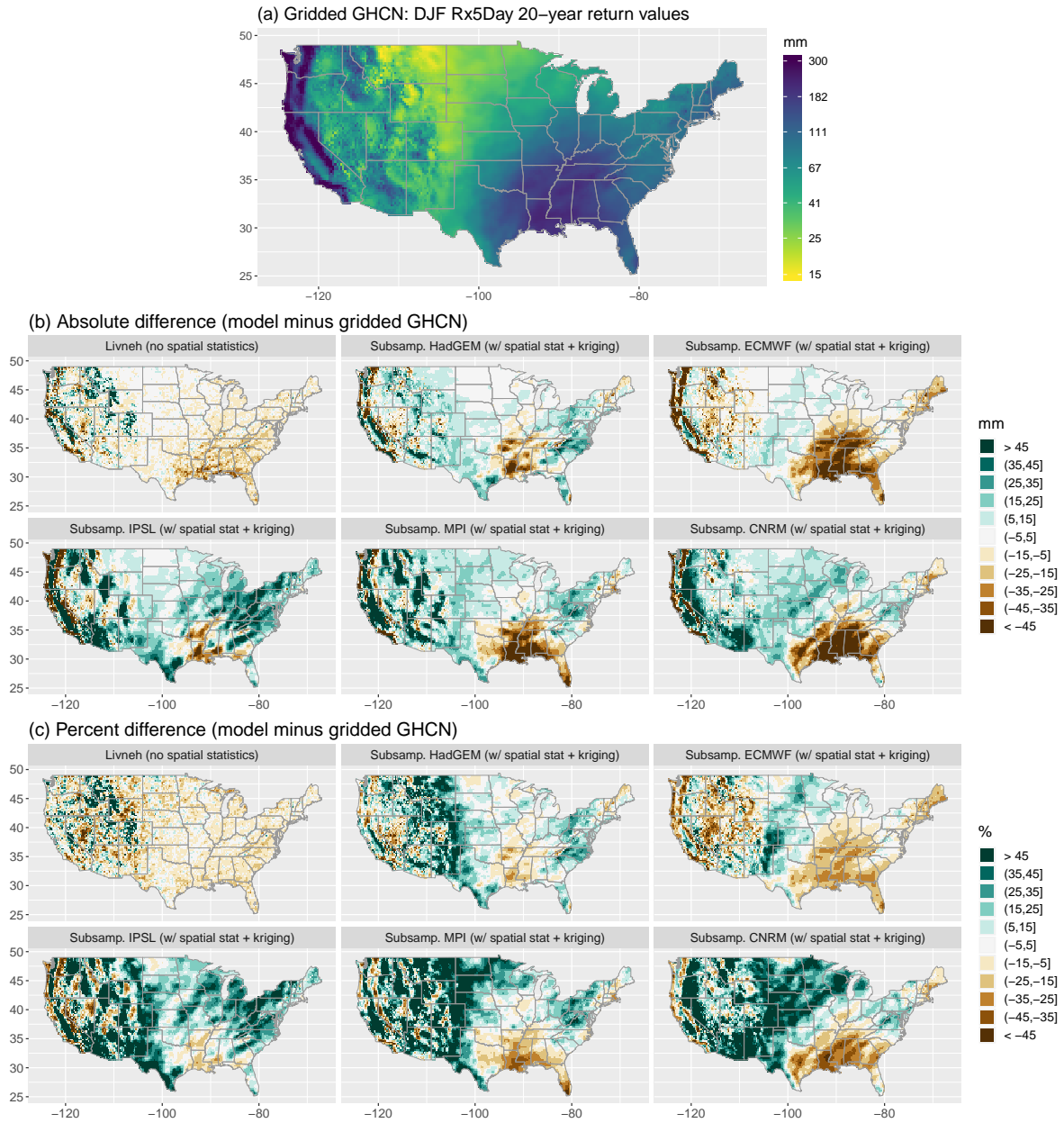


Figure A.3: Gridded estimates of 20-year return values (for Rx5Day in DJF; mm) from the GHCN station data using the methodology of [Risser et al. \(2019b\)](#) (panel a.). Panels b. and c. show the absolute difference and percent difference, respectively, between the GHCN estimates and the estimates obtained from the [Livneh et al. \(2014\)](#) data product and models. The Livneh comparison is based on the estimates shown in Figure A.2; otherwise, the model comparisons use the estimates calculated from the subsampled model data using the [Risser et al. \(2019b\)](#) methodology to do spatial smoothing and gridding/kriging. These maps are used to calculate the extreme bias in Figures 1 and 3 (although note that the limits on the color bars differ from this plot).

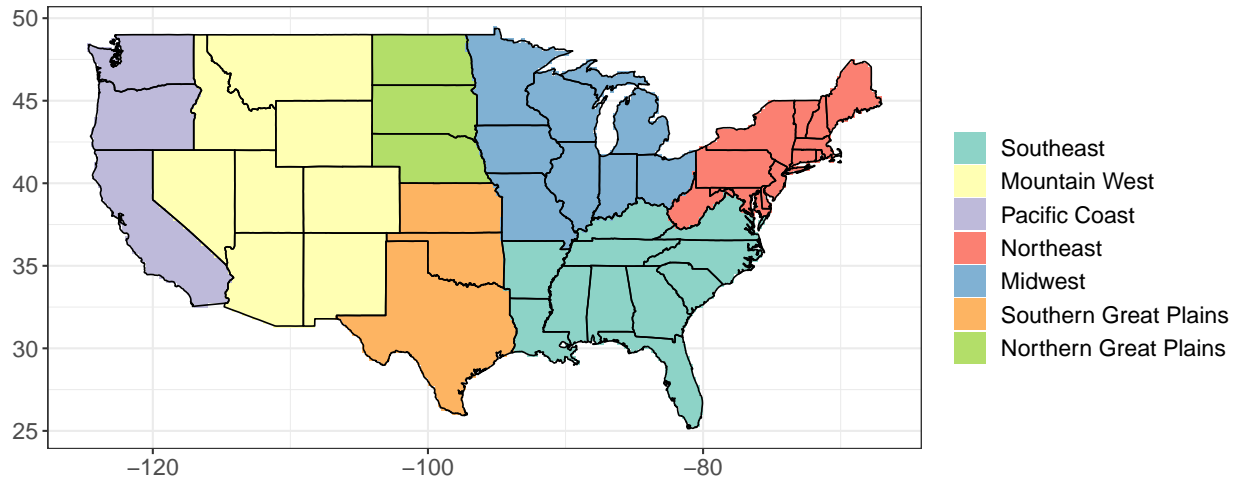


Figure A.4: The seven subregions used in our analysis. These are a slight variation on the regions defined in the Fourth National Climate Assessment.

Table A.1: The number of GHCN weather stations (of the original $n = 5202$ considered) and 0.25° grid cells in each subregion as well as their ratio (number of stations divided by number of grid cells).

Subregion	Number of stations	Number of grid cells	Ratio
Southeast	1019	2087	0.49
Mountain West	902	3824	0.24
Pacific Coast	564	1436	0.39
Northeast	551	917	0.60
Midwest	948	2087	0.45
Southern Great Plains	803	1671	0.48
Northern Great Plains	415	1051	0.39
Total (CONUS)	5202	13073	0.40

Table A.2: Absolute extreme bias (in mm) and relative extreme bias (percent) for each climate model, integrated over Kansas and Utah for comparisons C1, C2, and C3. (Note: the bias values are shown graphically in Figure 1a and b).

<i>Kansas</i>						
Model	<i>Abs. extreme bias (mm)</i>			<i>Rel. extreme bias (%)</i>		
	C1	C2	C3	C1	C2	C3
ECMWF	6.98	2.20	6.60	12.77	3.70	11.51
IPSL	12.59	7.47	11.31	23.03	12.49	19.59
HadGEM	8.04	4.78	5.85	14.71	7.88	10.30
MPI	13.26	9.17	8.63	24.26	15.48	14.90
CNRM	22.22	16.56	19.66	40.64	27.21	33.78

<i>Utah</i>						
Model	<i>Abs. extreme bias (mm)</i>			<i>Rel. extreme bias (%)</i>		
	C1	C2	C3	C1	C2	C3
ECMWF	-13.55	-2.22	-7.63	-23.40	-4.52	-14.58
IPSL	9.52	28.39	16.39	16.44	58.19	32.27
HadGEM	5.29	24.97	12.19	9.14	49.35	23.50
MPI	24.20	47.49	34.14	41.78	102.38	70.36
CNRM	3.62	12.90	8.03	6.25	25.45	15.17

Table A.3: Taylor diagram skill scores, absolute extreme bias (in mm), and relative extreme bias (percent) for each climate model, integrated over CONUS and the subregions for comparisons C1, C2, and C3. The skill score has no units; values closer to 1 indicate higher skill. Furthermore, the skill scores are calculated after the absolute extreme bias has been removed. (Note: the bias values are shown graphically in Figure 3a and b).

<i>CONUS</i>									
	<i>Skill score (no units)</i>			<i>Abs. extreme bias (mm)</i>			<i>Rel. extreme bias (%)</i>		
Model	C1	C2	C3	C1	C2	C3	C1	C2	C3
ECMWF	0.83	0.85	0.88	-7.39	-9.75	-10.53	-8.74	-10.69	-12.01
IPSL	0.74	0.67	0.74	21.27	20.49	18.50	25.15	22.90	21.38
HadGEM	0.90	0.90	0.93	8.06	7.24	4.46	9.53	7.65	5.08
MPI	0.78	0.72	0.78	14.37	11.97	11.39	16.99	13.03	13.08
CNRM	0.82	0.81	0.85	6.92	3.10	4.10	8.18	3.38	4.69

<i>Southeast</i>									
	<i>Skill score (no units)</i>			<i>Abs. extreme bias (mm)</i>			<i>Rel. extreme bias (%)</i>		
Model	C1	C2	C3	C1	C2	C3	C1	C2	C3
ECMWF	0.77	0.73	0.79	-17.52	-30.65	-30.01	-12.48	-19.99	-19.65
IPSL	0.67	0.62	0.69	22.19	8.91	9.35	15.80	5.81	6.13
HadGEM	0.72	0.71	0.77	12.39	-1.01	-1.06	8.83	-0.66	-0.69
MPI	0.61	0.56	0.60	-7.23	-20.55	-20.95	-5.15	-13.29	-13.59
CNRM	0.51	0.46	0.48	-17.36	-31.02	-31.03	-12.36	-20.16	-20.16

<i>Mountain West</i>									
	<i>Skill score (no units)</i>			<i>Abs. extreme bias (mm)</i>			<i>Rel. extreme bias (%)</i>		
Model	C1	C2	C3	C1	C2	C3	C1	C2	C3
ECMWF	0.59	0.83	0.83	-7.06	3.20	-3.19	-12.91	7.13	-6.34
IPSL	0.61	0.51	0.63	13.63	24.59	19.55	24.92	55.12	40.34
HadGEM	0.70	0.78	0.84	4.89	16.81	8.81	8.94	36.85	17.48
MPI	0.66	0.54	0.65	17.69	29.29	23.80	32.36	65.91	49.34
CNRM	0.70	0.75	0.81	12.84	22.49	17.18	23.49	50.75	34.78

<i>Pacific Coast</i>									
	<i>Skill score (no units)</i>			<i>Abs. extreme bias (mm)</i>			<i>Rel. extreme bias (%)</i>		
Model	C1	C2	C3	C1	C2	C3	C1	C2	C3
ECMWF	0.72	0.72	0.80	-29.82	-24.52	-30.37	-19.31	-15.39	-19.74
IPSL	0.58	0.46	0.53	40.00	55.78	41.38	25.89	35.65	27.88
HadGEM	0.85	0.81	0.88	2.47	23.19	1.57	1.60	14.05	1.01
MPI	0.68	0.59	0.67	44.23	66.04	44.54	28.63	41.15	29.48
CNRM	0.72	0.72	0.81	4.85	11.65	9.02	3.14	7.25	5.98

Table A.4: (continued) Taylor diagram skill scores, absolute extreme bias (in mm), and relative extreme bias (percent) for each climate model, integrated over CONUS and the subregions for comparisons C1, C2, and C3. The skill score has no units; values closer to 1 indicate higher skill. Furthermore, the skill scores are calculated after the absolute extreme bias has been removed. (Note: the bias values are shown graphically in Figure 3a and b).

<i>Northeast</i>									
	<i>Skill score (no units)</i>			<i>Abs. extreme bias (mm)</i>			<i>Rel. extreme bias (%)</i>		
Model	C1	C2	C3	C1	C2	C3	C1	C2	C3
ECMWF	0.46	0.47	0.58	-3.87	-8.54	-9.17	-4.51	-9.37	-10.04
IPSL	0.47	0.47	0.47	32.13	26.79	25.62	37.47	29.40	27.93
HadGEM	0.65	0.69	0.71	12.72	8.74	6.70	14.84	9.58	7.28
MPI	0.46	0.47	0.55	16.02	11.05	11.10	18.69	12.18	12.25
CNRM	0.55	0.54	0.62	7.61	3.39	2.57	8.88	3.74	2.82

<i>Midwest</i>									
	<i>Skill score (no units)</i>			<i>Abs. extreme bias (mm)</i>			<i>Rel. extreme bias (%)</i>		
Model	C1	C2	C3	C1	C2	C3	C1	C2	C3
ECMWF	0.93	0.89	0.93	0.72	-3.67	-3.64	1.05	-4.92	-4.99
IPSL	0.91	0.90	0.93	21.15	17.63	17.35	30.84	23.85	23.87
HadGEM	0.96	0.95	0.97	5.58	1.19	1.60	8.14	1.56	2.20
MPI	0.95	0.93	0.96	10.27	5.22	5.75	14.98	6.94	7.83
CNRM	0.92	0.89	0.92	14.99	10.13	9.99	21.86	13.49	13.63

<i>Southern Great Plains</i>									
	<i>Skill score (no units)</i>			<i>Abs. extreme bias (mm)</i>			<i>Rel. extreme bias (%)</i>		
Model	C1	C2	C3	C1	C2	C3	C1	C2	C3
ECMWF	0.92	0.87	0.90	0.90	-4.49	-4.06	1.12	-5.17	-4.72
IPSL	0.90	0.87	0.91	18.81	12.78	13.78	23.38	14.64	16.00
HadGEM	0.94	0.92	0.95	12.54	5.33	7.32	15.59	5.83	8.57
MPI	0.90	0.87	0.89	9.19	1.47	1.99	11.43	1.65	2.31
CNRM	0.79	0.73	0.76	8.16	1.13	2.23	10.15	1.27	2.58

<i>Northern Great Plains</i>									
	<i>Skill score (no units)</i>			<i>Abs. extreme bias (mm)</i>			<i>Rel. extreme bias (%)</i>		
Model	C1	C2	C3	C1	C2	C3	C1	C2	C3
ECMWF	0.84	0.77	0.92	4.80	2.95	3.38	15.52	8.75	10.26
IPSL	0.82	0.81	0.91	6.75	5.14	5.15	21.80	15.63	15.66
HadGEM	0.86	0.81	0.92	4.14	2.41	2.76	13.37	7.02	8.50
MPI	0.70	0.60	0.76	13.63	11.55	11.49	44.06	34.52	35.02
CNRM	0.79	0.78	0.85	14.32	12.18	12.15	46.29	35.75	36.85